In Silico Phase-Contrast X-Ray Imaging of Anthropomorphic Voxel-Based Phantoms

Ilian Häggmark, Kian Shaker, and Hans M. Hertz

***Abstract*— Propagation-based phase-contrast X-ray imaging is an emerging technique that can improve dose efficiency in clinical imaging. *In silico* tools are key to understanding the fundamental imaging mechanisms and develop new applications. Here, due to the coherent nature of the phase-contrast effects, tools based on wave propagation (WP) are preferred over Monte Carlo (MC) based methods. WP simulations require very high wave-front sampling which typically limits simulations to small idealized objects. Virtual anthropomorphic voxel-based phantoms are typically provided with a resolution lower than imposed sampling requirements and, thus, cannot be directly translated for use in WP simulations. In the present paper we propose a general strategy to enable the use of these phantoms for WP simulations. The strategy is based on upsampling in the 3D domain followed by projection resulting in high-resolution maps of the projected thickness for each phantom material. These maps can then be efficiently used for simulations of Fresnel diffraction to generate *in silico* phase-contrast X-ray images. We demonstrate the strategy on an anthropomorphic breast phantom to simulate propagation-based phase-contrast mammography using a laboratory micro-focus X-ray source.**

***Index Terms*— In silico imaging, mammography, phase contrast, radiography, wave propagation, x-ray.**

I. Introduction

PHASE-CONTRAST X-ray imaging is a collection of methods that provide superior soft-tissue contrast compared to conventional absorption-based X-ray imaging. Simulations based on wave propagation (WP) are critical to develop and understand these novel imaging methods. The imposed requirement of micrometer-level wave-front sampling is in direct contradiction to the need for clinically relevant large field-of-view simulations of anthropomorphic virtual phantoms. In the present paper we demonstrate a strategy for bridging the gap between these length-scales, and demonstrate WP simulations on a virtual breast model to simulate propagation-based phase-contrast mammography.

For certain imaging tasks, phase-contrast X-ray imaging provides higher contrast at lower radiation dose [1]. The techniques rely on detecting the phase shift of transmitted X-rays caused by the imaged object in addition to the conventional attenuation. One particular sub-technique, propagation-based imaging (PBI), has the advantage of a straightforward experimental arrangement with no need for X-ray optical components. It is also compatible with small and relatively inexpensive laboratory sources and commercially available detectors [2]. One PBI application is mammography, which has been developed at synchrotron facilities for over 20 years [3]–[5]. Clinical trials have shown an improved sensitivity and specificity [6]. Laboratory systems, a prerequisite for large scale screening, have been investigated both for PBI [7], [8] and grating-based techniques [9]–[11].

In silico tools are extensively used in X-ray imaging to investigate new methods and optimize imaging tasks. Simulations of X-ray transport are typically divided into methods based on either Monte Carlo (MC) or wave propagation (WP). The two different approaches arise from the wave-particle duality of electromagnetic radiation. The MC approach accurately models the statistical interactions (e.g., scattering, absorption) between photons and materials. However, coherent effects arising from the wave-nature of the radiation (e.g., diffraction, interference) cannot be captured in this particle-view. To accurately model these effects, simulations based on WP are necessary. Therefore, despite a wide range of available MC codes for X-ray transport (e.g., PENELOPE [12], Geant4 [13], FLUKA [14]) none are directly suitable for simulating PBI. A few attempts at combining the particle and wave models to simulate phase-contrast imaging have been demonstrated. One approach is simulating refraction in an MC framework, either by applying Snell's law on individual photons passing through material interfaces in the object [15] or by tracking the distances travelled by each photon through the different materials so that a phase may be assigned to each photon reaching the detector in a post-processing step [16]. Another approach is dividing the simulation into two segments where MC is used to track photons through the object and WP to simulate coherent effects in the propagation between object and the detector [17]. Nevertheless, these approaches require that objects are defined by simplified analytical shapes, making their application to realistic models with complex morphology challenging.

The recent surge of interest in virtual clinical trials (VCTs) in medical imaging [18] relies to a significant degree on the development of realistic virtual models of human anatomy. Whole-body models (e.g., Virtual Population [19], XCAT [20]) are widely used for investigation of a large

Manuscript received July 6, 2020; revised October 5, 2020; accepted October 12, 2020. Date of publication October 15, 2020; date of current version February 2, 2021. This work was supported by the Knut and Alice Wallenberg Foundation. *(Corresponding author: Ilian Häggmark.)*

The authors are with the Department of Applied Physics, KTH Royal Institute of Technology/AlbaNova, 10691 Stockholm, Sweden (e-mail: ilian.haggmark@biox.kth.se; kiansd@kth.se; hertz@biox.kth.se).

Color versions of one or more of the figures in this article are available online at https://ieeexplore.ieee.org.

Digital Object Identifier 10.1109/TMI.2020.3031318

range of morphological and molecular imaging techniques. Models of isolated organs with a higher degree of detail such as the brain [21] and breast [22] can be used to investigate region-specific imaging tasks. These models can be generated by a wide range of means, from analytical generation based on anthropomorphic modelling to direct extraction from experimental imaging datasets. When it comes to storing and representation, options are more limited. Most virtual models consist either of mathematically represented surfaces (e.g., non-uniform rational basis spline, NURBS) [23], [24] or more often as discretized volumes (e.g., based on polygon mesh or voxels). Voxel-based discretized models are the most common, partly due to their shared format with experimental data allowing similar processing. The main advantage of voxelized models is the relatively uncomplicated incorporation into numerical simulations of, e.g., X-ray transport. The main disadvantage is the cubic growth of storage space with resolution. This effectively limits high-resolution simulations of imaging tasks. One such imaging tasks is phase-contrast X-ray imaging. Here, accurate WP simulations require micrometer model sampling, in direct contradiction with the aforementioned scaling of voxelized models. Previous work on WP simulations has been limited by this sampling requirement [25], [26].

In the present paper we demonstrate a strategy for combining voxelized models of human anatomy with the micrometer sampling requirements of WP simulations for *in silico* phase-contrast X-ray imaging. The strategy allows us to perform unprecedented microscale wave-front simulations of clinically relevant macroscale field-of-views. We discuss the challenges associated with high-resolution voxelized volumes and show how high-resolution data can be generated from coarse resolution virtual anatomic models. The strategy is demonstrated on an anthropomorphic breast phantom allowing us to perform realistic simulations of propagation-based X-ray phase-contrast mammography. We use our simulations to investigate the potential of state-of-the-art laboratory sources for mammography and discuss possible challenges related to the experimental realization.

II. Methods

A. Sampling Requirement in Wave-Propagation Simulations

Fresnel diffraction is the main effect in PBI and thus the core of any *in silico* PBI imaging tool. It can be efficiently evaluated numerically using the convolution approach. In practice, this consists in a multiplication in Fourier space between the transmission function (calculated from object properties) and the Fresnel propagator $h(x, y)$ [27]. In Fourier space the propagator is given by

$$H(u, v) = \mathfrak{F}\{h(x, y)\} = \exp(-iz\lambda\pi(u^2 + v^2)), \qquad (1)$$

where λ is the X-ray wavelength, z is the propagation distance and (u, v) the spatial frequencies corresponding to the wave-front spatial coordinates (x, y). $H(u, v)$ is illustrated in Fig. 1. We note that $H(u, 0)$ (cf. Fig. 1(b)) is equivalent to the contrast transfer function (CTF) in the context of propagation-based phase-contrast X-ray imaging [28]. To simulate phase contrast, we want to include the direct imaging regime, i.e., the central frequency range in Fig. 1(b) where the phase part of CTF is positive [29]. Without loss of generality, considering the 1D case ($v = 0$) translates into a criterion stating that frequencies up to $\mathrm{Im}\{H(u = u_{\max})\} = 0$ have to be included, i.e.,

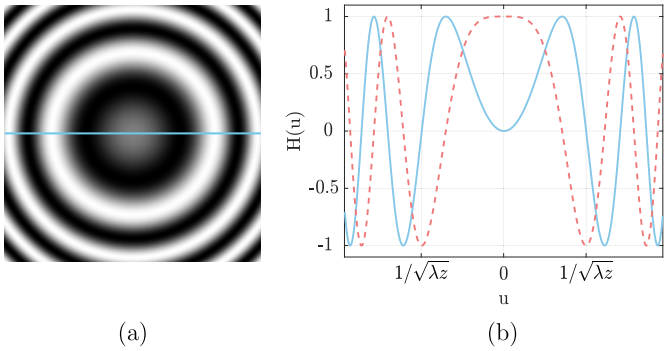

Fig. 1. Fresnel propagator given in Eq. (1) with maximum frequency set by $1/(2\Delta x)$ (here: $\Delta x = 1$ μm), $\lambda = 0.5$ Å and $z = 0.3$ m. (a) Imaginary part. (b) Line profile of real part (dashed) and negative imaginary part (solid) of the propagator at $v = 0$. The real and imaginary parts corresponds to absorption and phase effects, respectively.

$$\mathrm{Im}\{\exp(-iz\lambda\pi u_{\max}^2)\} = \sin(-z\lambda\pi u_{\max}^2) = 0. \qquad (2)$$

Here, Im signifies the imaginary part. The last equality is fulfilled when the sine argument is a multiple of π, first occurring when $z\lambda u_{\max}^2 = 1$. Furthermore, in discrete calculations the maximum spatial frequency in Fourier space is given by $u_{\max} = 1/(2\Delta x)$, where Δx is the sampling in the spatial domain [27]. Combining these results, we obtain a simple sampling criterion,

$$\Delta x < \frac{\sqrt{\lambda z}}{2}. \qquad (3)$$

The numerator $\sqrt{\lambda z}$ can be interpreted as the width of the first Fresnel zone or Fresnel fringe [30]. For typical hard X-ray wavelengths, e.g., 0.5 Å (~25 keV) and propagation distances larger than 0.3 m, this translates into a requirement of sub-2-μm wave-front sampling. If the latter is not fulfilled, the phase-contrast effects are underestimated. Furthermore, the transmission function must match the propagator sampling, otherwise artifacts can be introduced. A lower sampling of the transmission function can, e.g., lead to edge enhancement between the coarse voxels.

To facilitate WP simulations, the projection approximation can be used [29]. The latter is based on the assumption of negligible divergence of X-rays within the object and is a good approximation when the object thickness is small compared to the propagation distance [31]. This is a powerful approximation that, if exploited correctly, can reduce computational time and data storage several orders of magnitude [32].

B. Upsampling of Anthropomorphic Breast Phantom

In this section, we demonstrate our upsampling strategy on a realistic breast model [22]. The model was initially developed

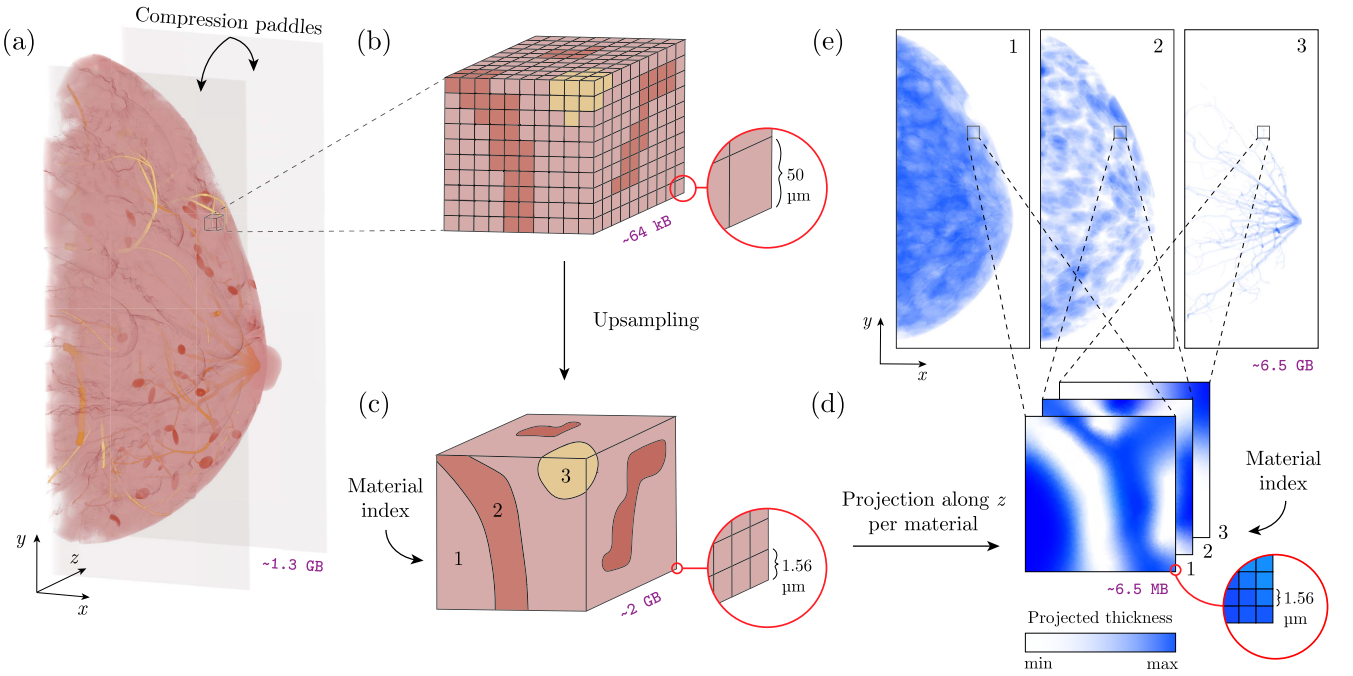

Fig. 2. Schematic demonstrating the strategy for processing voxel-based anthropomorphic phantoms for phase-contrast X-ray imaging simulations. The strategy is demonstrated on a breast phantom. (a) 3D visualization of an anthropomorphic breast phantom [22]. The compression paddles used in mammography are also visible and part of the voxelized volume. This specific breast phantom represents a breast classified as dense (see Sec. II-B for details) with a size of ∼4×10×4 cm in the *x,y,z* directions, respectively. The resolution of the voxelization is 50 μm resulting in a total of ∼800 × 2000×800 voxels and storage size of ∼1.3 GB for the whole phantom at one byte per voxel. (b) Subvolume of ∼40 × 40×40 voxels (∼64 kB) extracted from the original phantom. The subvolume includes different material regions denoted with different indices. (c) As described in Sec. II-B, each subvolume is upsampled 32 times to 1.56 μm voxelization. Accordingly, subvolume storage size expands by a factor 32^3 into ∼2 GB. Sharp boundaries between different material regions are preserved in the upsampling procedure. (d) The upsampled volume is projected in the X-ray direction to obtain a high-resolution 2D map of the projected thickness of each material constituent. Storage size of the subvolume 2D map reduces to ∼6.5 MB. (e) The procedure is repeated for each subvolume in the original phantom to produce a 2D map of the projected thickness of each material for the whole breast phantom. The final storage size of each high-resolution material map is ∼6.5 GB.

for the Virtual Imaging Clinical Trials for Regulatory Evaluation (VICTRE) project by the American Food and Drug Administration (FDA) [33]. Here we use a sample breast phantom provided by the VICTRE project, consisting of a dense breast (60% glandular volume) compressed for a craniocaudal view with a lateral size of ∼4×10 cm and thickness of 4 cm. A breast phantom with high glandular fraction was chosen as these are considered diagnostically challenging in state-of-the-art mammography. The phantom is generated at a 50-μm voxelization (see Fig. 2(a)). The phantom includes a total of 10 separate anatomical components, such as fatty tissue, glandular tissue, connective tissue (i.e., Cooper ligaments), the ductal network including terminal ductal lobular units (TDLUs), the vascular network and calcifications. The latter were between 150 and 250 μm in diameter. Additionally, spiculated lesions of roughly 8 mm diameter are present at 4 different locations.

To use the phantom for WP simulations of PBI mammography, the wave-front sampling criterion has to be fulfilled by the phantom as well. In fact, the resolution of the phantom voxelization is one of the major bottle-necks for accurate WP simulations. At the 50-μm sampling described above, assuming at least one byte of memory required to represent the local material properties, the breast phantom requires a minimum storage size of ∼1.3 GB. Similarly, at 2-μm voxelization, 20 TB of RAM is theoretically needed to store the whole phantom in memory which causes problems even with modern computer architectures. Here, the projection approximation described earlier can be exploited to remove the need for storing the whole phantom in 3D. One naive approach would therefore be to project the breast phantom in the X-ray direction at the coarse voxelization to acquire a "thickness map" in 2D for each material at 50-μm sampling, and then perform interpolation in the projection domain to obtain the required sub-2-μm wave-front sampling. Unfortunately, conventional interpolation schemes (i.e., linear, cubic, spline) in the projection domain inevitably causes smoothing of the boundaries between different material compartments. This in turn directly affects the ability to simulate the phase-contrast edge-enhancement, which relies on accurate representation of material boundaries in the phantom. This has limited previous simulations of phase-contrast X-ray mammography [25], [26].

To circumvent the challenges related to data storage and the sharpness of material boundaries, we have developed a strategy for phantom upsampling from a coarse voxelization (here 50 μm) to the required wave-front sampling (here sub-2-μm). The core idea is interpolation in the 3D domain followed by exploitation of the projection approximation where the processing steps have been carefully designed so that material boundaries are preserved to allow for accurate simulations of

phase-contrast edge-enhancement. Furthermore, the strategy is designed to reduce memory overhead allowing for parallelization which can be adapted to the RAM available. The different steps are visually represented in Fig. 2, and described in detail below:

1) **Subvolume extraction.** To reduce memory overhead, subvolumes of typically $40\times40\times40$ voxels are extracted at the coarse voxelization (here 50 μm) and further processed individually. The number of subvolumes processed in parallel can be tuned to the available RAM. Each subvolume is then padded in all dimensions to ensure that material boundaries spanning adjacent subvolumes are not mismatched in the following processing steps. For each subvolume, the materials are separated into individual subsets, containing only the index of the material in question and with zeros for the rest.
2) **Smoothing.** 3D Gaussian smoothing is applied to each material subset to soften the feature edges, thus eliminating traces of the coarse voxelization. The Gaussian parameters are tuned for each material separately to ensure that the morphology of the features is preserved.
3) **Upsampling.** Each material subset is upsampled by a factor (here 32) using tricubic interpolation to the final voxelization (here 1.56 μm).
4) **Edge preservation.** Thresholds are applied to the upsampled material subsets to recreate the sharp boundaries. As default, thresholds are chosen corresponding to half of the value of the original material index. The thresholds can be tuned to make sure that small features, such as calcifications, do not disappear completely.
5) **Re-combination.** The padding added earlier is removed from the upsampled subsets, which are then re-combined into a single subvolume in order of largest to smallest feature, to avoid any voids appearing in the final upsampled subvolume as well as small features being replaced by the larger features. The latter may occur as the smoothing, upsampling, and thresholding can cause the material boundaries to slightly shift in space.
6) **Projection.** The re-combined upsampled subvolume is projected in the desired direction(s) to acquire a 2D map of the projected thickness for each material separately. These maps are inserted into the corresponding location of the complete phantom.

The steps above are repeated for all subvolumes resulting in 2D material maps of the whole phantom at the required wave-front sampling (here 1.56 μm, cf. Fig. 2(e)). By dividing the voxelized phantom into subvolumes and processing them individually we circumvent the need for storing the whole upsampled phantom in RAM at any given time. Choosing the Gaussian smoothing parameter, the thresholds and the recombination order is done manually, but values chosen for a representative subvolume will typically work well for the rest of the subvolumes.

Upsampling of the dense breast phantom (cf. Fig. 2(a)) was performed using code written in Matlab (R2019b, MathWorks, US) executed at the PDC Center for High Performance Computing at KTH Royal Institute of Technology, on a node with 2 TB RAM and 4 Intel E7-8857v2 CPUs with a total of 48 CPU cores. The entire procedure took 70 hours to complete where 40 subvolumes were processed in parallel on different cores. CPU usage of each core was typically high during the whole procedure (>90%). The maximum memory usage during processing was 800 GB, 20 GB for each subvolume and core. The storage size of the final upsampled 2D projection map is ~6.5 GB for each of the 10 separate materials.

C. Propagation-Based Phase-Contrast Simulations

Simulations of propagation-based phase-contrast imaging by the Fresnel diffraction integral have previously been shown to correspond well to experimental data [34]. The core of the simulation is the WP which is performed using the convolution approach. The transmission function $g(x, y)$ is convolved through Fourier-space multiplication with the Fresnel propagator $h(x, y)$ (see Eq. (1)) to calculate the X-ray intensity $I(x, y)$ at the detector,

$$I(x, y) \propto \left(\mathfrak{F}^{-1}\{\mathfrak{F}\{g(x, y)\} \cdot H(u, v)\}\right)^2. \tag{4}$$

The Fourier transform and its inverse is denoted by $\mathfrak{F}$ and $\mathfrak{F}^{-1}$, respectively. The transmission function describes the attenuation and phase shift at each position immediately behind the object,

$$g(x, y) = \left[\prod_n \exp\left(-\mu_n(E) \cdot T_n(x, y)/2\right)\right] \cdot \exp\left(i\frac{2\pi}{\lambda}\sum_n -\delta_n(E) \cdot T_n(x, y)\right), \tag{5}$$

where $g(x, y)$ is calculated from the projected material thicknesses $T_n(x, y)$ together with the parameters $\delta_n(E)$ and $\mu_n(E)$ at the X-ray energy E for each of the n materials. For the materials in the breast phantom simulated in this article, $\delta_n(E)$ is calculated from RTAB [35] and $\mu_n(E)$ is identical to those used in the VICTRE project [33].

Equation (4) gives an ideal image that must be scaled according to experimental parameters. The intensity recorded by the detector is energy-dependent and varies with the source spectrum, filters, experimental geometry, and detector absorption efficiency. Next, the image has to be convolved with the system point-spread-function (PSF) to account for the source spot size and detector blurring. After resampling the images to the physical pixel sizes, Poisson noise is added to model photon statistics. The number of photons reaching each pixel is known from the flux and the geometry. The whole workflow is schematically shown in Fig. 3. The five first steps of the WP part are repeated over multiple monochromatic segments to simulate a polychromatic spectrum. This can also be performed on subsections of the field-of-view if RAM is limited. Read-out noise and other aspects of the detector model can be incorporated if desired. The code performing the WP simulation is written in Matlab (R2019b, MathWorks, US).

D. Validation Against Monte Carlo Simulations

To evaluate the accuracy of our WP simulations we compared them to Monte Carlo simulations, the gold standard

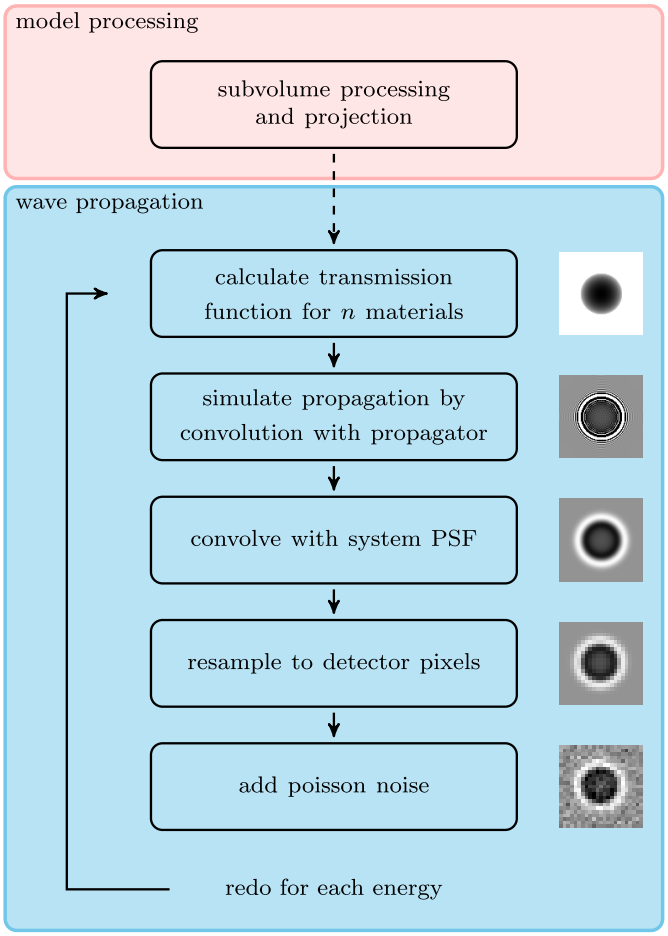

Fig. 3. Schematic of the full simulation workflow. The WP section can be repeated for multiple energies to simulate a polychromatic X-ray source. The core of the WP simulation is shown in five steps with corresponding image of the result.

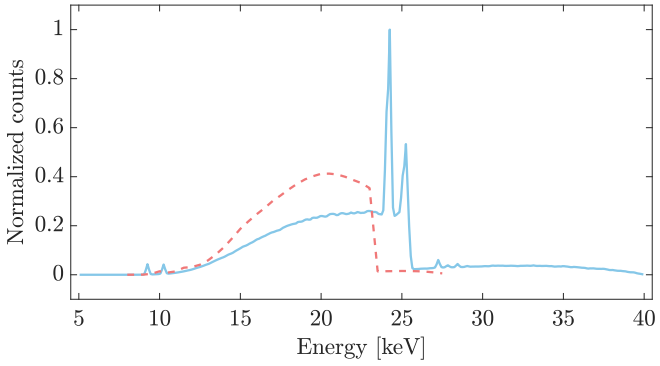

Fig. 4. X-ray emission spectra for the two modelled sources. Dashed line (red) shows the conventional mammography source used for validation in Sec. II-D. The solid line (blue) shows the liquid-metal-jet source used for demonstration of the phase-contrast simulations. The spectra are scaled so the total photon count is equal.

TABLE I
PARAMETERS FOR SIMULATED IMAGING GEOMETRIES

Parameter	Screening	PBI		
R_1 [m]	0.65	1	4	10
R_2 [m]	0	1	4	10
z_{eff} [m]	0	0.5	2	5
M	1	2	2	2
source spot (d) [µm]	300	20	20	20
detector pixel-size [µm]	50			
detector PSF [µm]	75			

for simulations of X-ray transport. For this purpose, we used the state-of-the-art and highly-accelerated MC-GPU code (version 1.5b) [36] which is a part of the VICTRE pipeline [33]. As MC-GPU does not model the phase-contrast phenomena, the evaluation was performed in a conventional screening mammography setting. Here, the distance between X-ray source and detector was set to 65 cm, and the breast phantom was placed right in front of the detector. The modelled X-ray source was a tungsten X-ray tube with a 300 μm emission spot, acceleration voltage of 28 kVp and a 50 μm rhodium filter plus a 1 mm beryllium window (cf. Fig. 4 for emission spectrum) [37]. A conventional direct conversion detector for mammography was modelled with 200 μm thick amorphous selenium as detection material and pixel sizes of 50 μm [38]. A detector field of view of 25 $\times$ 12.5 cm was sufficient to cover the breast phantom. An ideal anti-scatter grid was simulated by neglecting detector signal contribution from X-ray scattering. Parameters for the imaging geometry are summarized in Table I.

As MC-GPU provides a dose estimate, the number of X-ray photons simulated for both MC and WP simulations were tuned for a mean glandular dose (MGD) of 1.5 mGy which is a typical dose within the recommendations of international organizations for mammographic screening [39]. The resulting number of X-ray photons simulated through the breast was $8.9 \cdot 10^{10}$ distributed across the emission spectrum. The WP simulations of the processed model were carried out on a desktop computer with 128 GB RAM and an Intel Core i9-9920X CPU. For the WP simulations the emission spectrum was divided into 10 energy bins simulated as monochromatic segments. A simulated mammogram of the upsampled and projected breast phantom (cf. Fig. 2) took ~4 min per energy bin for a total of ~40 min. MC simulations of the original breast phantom (50-μm voxelization) were carried out with MC-GPU on another computer with a NVIDIA GTX1060 GPU, producing the same simulated mammogram with equal number of X-ray photons in ~46 min. The MC simulation speed was thus $\sim 3.2 \cdot 10^7$ X-ray photons/s, including overhead. Comparison of the result is done in Sec. III-A.

E. Laboratory Propagation-Based Mammography

To demonstrate the suggested simulation strategy, we consider laboratory PBI mammography. With source-to-object and object-to-detector distances given by R_1 and R_2 respectively, the magnification is $M = (R_1 + R_2)/R_1$. The spatial blurring D on the detector due to finite emission spot d is $D = d(M-1)$ (cf. Fig. 5). Typically, pixel sizes in state-of-the-art mammography units are 50-100 μm [38], whereas emission spots for conventional mammography are in the range of 100-300 μm [40]. State-of-the-art micro-focus sources can provide emission spots in the 10-μm-range, resulting in negligible spatial blurring at current detector pixel sizes and few-times

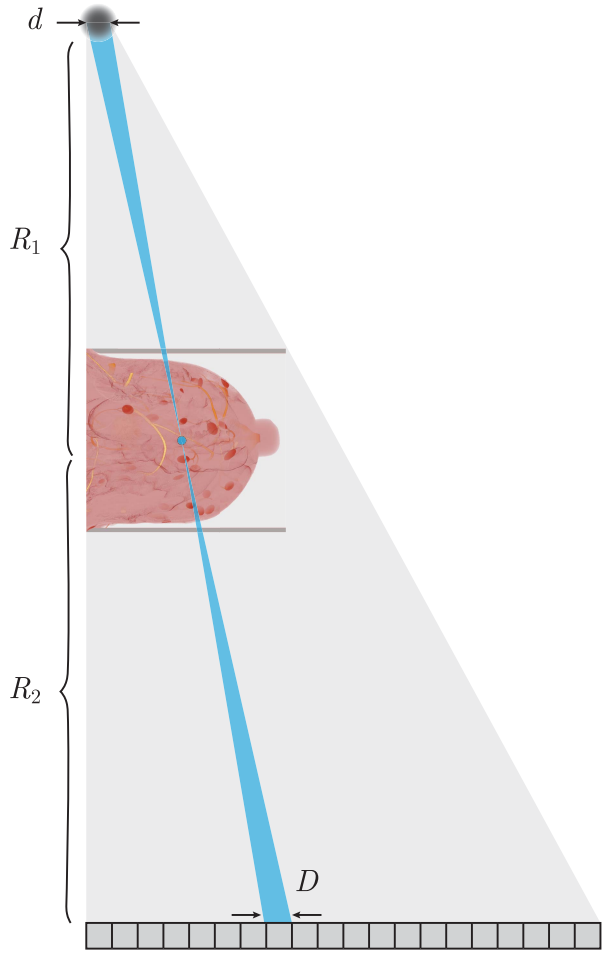

Fig. 5. Imaging geometry for magnified-view mammography which is also suitable for propagation-based phase-contrast imaging. R_1 is the distance between the X-ray emission spot and the compressed breast, R_2, is the distance to the image sensor. The finite emission spot size, here denoted as d results in the geometric blurring D on the image sensor.

magnification. In the present paper we model the liquid-metal-jet X-ray source (D2+, Excillum AB, Sweden) which is the brightest micro-focus source on the market [41]. The apparent X-ray emission spot was set to 20 μm full width at half maximum (FWHM). At 40 kVp acceleration voltage the source was set to the maximum electron-beam power of 140 W. The spectrum was filtered by 50 μm silver and 200 μm beryllium.

The propagation distance z is central to the edge enhancement in PBI [2]. In a parallel geometry the propagation distance z is equal to R_2, whereas in a cone-beam setup an *effective propagation distance* is used, given by [42]

$$z_{\text{eff}} = \frac{R_2}{M}. \tag{6}$$

For the present energy range and object feature sizes (100-μm-range) a fairly large z_{eff} is optimal. The magnification was here set to 2. The X-ray flux was varied accordingly for different R_1 to maintain a constant MGD of 1.5 mGy. Simulations were performed at effective propagation distances of 0.5 m, 2 m, and 5 m as described in Table I. Densities of materials in the breast phantom were obtained from the VICTRE project [33]. The calcifications were simulated as calcium oxalate (CaC_2O_4) with a density of 2.12 g/cm^3. The lesions in the breast phantom were simulated as glandular tissue with ~6% higher density, 1.1 g/cm^3 instead of nominal value of 1.035 g/cm^3, which is within the range previously reported [43], [44].

III. Results

A. Validation of Simulation Strategy

Figure 6 shows simulated mammograms corresponding to a screening scenario ($M = 1$) generated through both MC and WP approaches as described in Sec. II-D. The grayscale values displayed correspond to the optical depth (OD) defined as $-\ln(I/I_0)$, where I represents the transmitted intensity recorded with sample and I_0 without. In the absence of phase-contrast effects, i.e., $z_{\text{eff}} = 0$, the OD reflects the projected linear attenuation coefficient μ along the X-ray direction. Qualitatively we observe from Fig. 6 that the two approaches produce similar mammograms, confirming that our proposed WP approach can accurately produce *in silico* mammograms with the same level of realism as state-of-the-art MC simulations. There are minor relative displacements of the anatomical components due to both the difference in projection geometries (parallel-beam in WP and cone-beam in MC) and the phantom upsampling procedure for the WP simulation. The noise level in the WP simulation agrees with the MC, which was confirmed quantitatively by comparing the histograms of comparable regions.

Figure 7 shows a comparison of different sampling strategies for WP simulations and illustrates the importance of fulfilling the wave-front sampling requirements set by Eq. (3). A mammogram with $R_1 = R_2 = 4$ m is simulated, resulting in an effective pixel size of 25 μm and $z_{\text{eff}} = 2$ m. Three different sampling approaches that do not give accurate results are shown in Fig. 7(a)-(c). These create numerical artifacts that could be erroneously interpreted as real noise and the approaches in (a) and (b) cannot simulate edge enhancement. In (a) the sampling of $H(u, v)$ and $g(x, y)$ ($\Delta x = 50$ μm) is insufficient which results in low-frequency (grainy) noise. In (b) high propagator sampling ($\Delta x = 1.56$ μm) is used, but sampling of $g(x, y)$ is insufficient. To perform the multiplication between the two the propagator sampling is matched by 2D nearest-neighbor interpolation on the projected phantom. The nearest-neighbor interpolation scheme preserves the features of the original phantom, so that the only difference here compared to (a) is that the propagator fulfills the sampling requirement set by Eq. (3). $g(x, y)$ has, thus, smaller pixels, but all values within one 50-μm pixel are the same. In this case, artificial edge-enhancement will appear at 50-μm-intervals as this corresponds to the sharp transitions between adjacent voxels in the original phantom. When resampled back to the effective detector pixels (here 25 μm) this appears as high-frequency noise across the whole field-of-view. In (c) sufficient sampling is used in the propagator, but the high sampling in $g(x, y)$ is achieved through bicubic interpolation on the projected phantom. The high propagator sampling and interpolation produce edge enhancement, but

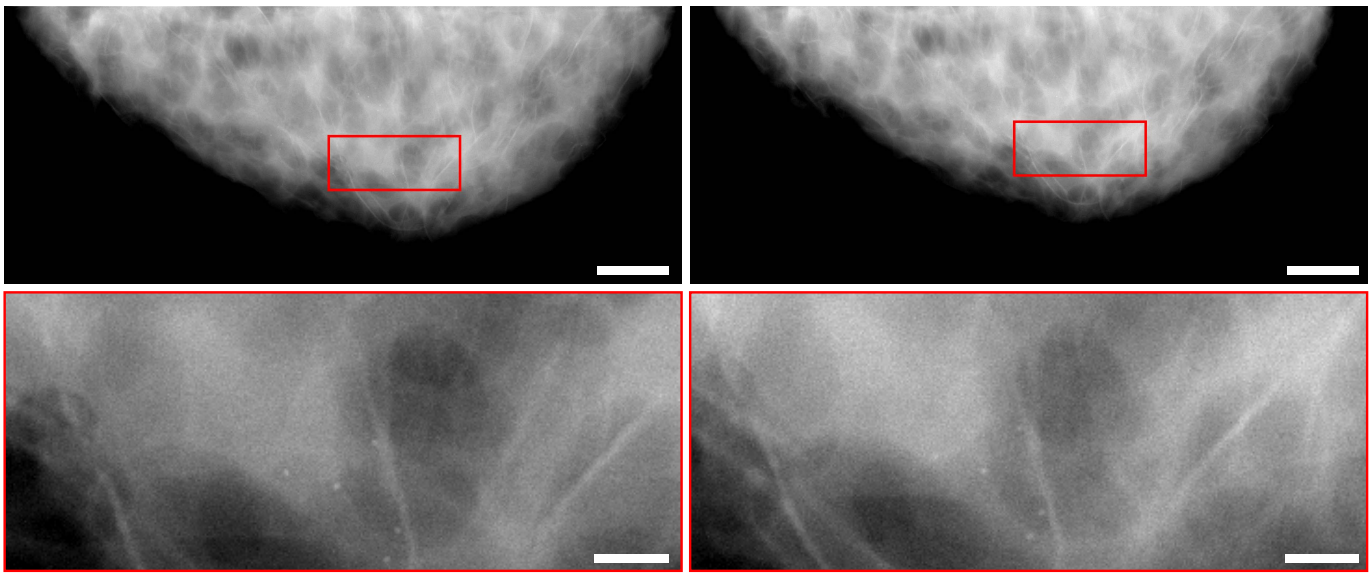

(a) (b)

Fig. 6. Comparison of MC and WP approaches for simulation of screening mammogram. Here R_1 is 65 cm and R_2 is 0 cm. (a) Mammogram generated from MC-GPU of the original phantom at 50-μm voxelization with a magnified section shown below. (b) Similar mammogram (overview and magnified section) generated through WP with the proposed upsampling strategy. Grayscale values are displayed as OD with windows set to [1.8, 2.8] and [2.1, 2.8] in the overview and magnified sections, respectively. Scale bars are 10 mm (overview) and 2 mm (magnified section). Darker regions are more fat-rich while brighter regions are made up of glandular and connective tissue. Calcifications in the 100-μm-range are visible as small bright spots in the magnified sections.

traces of the original 50-μm voxelation will give rise to noise as in (b). If the phantom is further smoothed to remove all traces of the 50-μm voxelation, too much blurring is introduced and smaller features as well as edge enhancement are lost. Finally, Fig. 7(d) shows our proposed upsampling strategy which accurately simulates the edge enhancement between materials without introducing any artifacts.

B. PBI Mammography Using Micro-Focus X-Ray Sources

Figure 8 shows simulations of PBI mammography with a liquid-metal-jet source. The impact of the effective propagation distance is readily visible in the magnified section (b)(e), (c)(f), and (d)(g) which corresponds to 0.5 m, 2 m, and 5 m respectively. The edge enhancement makes it possible to distinguish boundaries of various features such as Cooper ligaments (horizontal line in the center of (b)-(d)) and adipose regions (dark round structures). Visibility of calcifications is also improved. Arrows in (b)-(d) mark the positions of two 100-μm-range calcifications. In (b) they can hardly be seen, whereas they stand out very well in (d). A zoom in of a lesion is shown in (e)-(g). This is a spiculated mass, clinically often a sign of malignancy. In the case of dense breasts, as simulated here, lesions are significantly harder to locate [45]. Nevertheless, the spikes of the lesion are enhanced, making it easier to locate and characterize the lesion morphology with longer propagation distances.

The simulated flux, to keep the MGD constant at 1.5 mGy, grows as R_1^2. This translates into exposures times of 37 s, 10 min, and 1 h, respectively for the three propagation distances using the previously given settings for the simulated liquid-metal-jet X-ray source (see Sec. II-E).

IV. Discussion

We have shown how a straightforward upsampling strategy handles micrometer wave-front sampling in WP simulations and enables use of decimeter-sized anthropomorphic voxel-based phantoms for *in silico* PBI. We have furthermore given a criterion for sufficient wave-front sampling.

The computational strategy was demonstrated on a mammography application due to the availability of high-quality phantoms. However, the method is general. This is useful as more phantoms become available and phase-contrast imaging moves towards clinical imaging. With the increased interest in virtual clinical trials (VCTs) to evaluate medical imaging modalities [18], we show that our strategy opens up for VCT of phase-contrast imaging.

The sampling discussed in Sec. II-A puts a hard requirement on WP simulations. Figure 7 illustrates further that naive upsampling approaches, e.g., bicubic interpolation in 2D, are not sufficient. 3D interpolation is necessary which significantly increases computation time, although parallelization improves performance.

Some analytic models, like the presented one, can technically generate phantoms with arbitrary sampling. However, the memory requirements involved with direct phantom generation at micrometer-level sampling cannot be met with even the most powerful workstations.

An important feature of the proposed strategy is that upsampling is done only once for a phantom. Imaging parameters such as propagation distance, spectrum, dose or material parameters (δ and μ) etc. can be changed in the actual WP simulations. Even small modifications of the phantom can even be done, e.g., adding calcifications or lesions by adding and subtracting from the 2D maps.

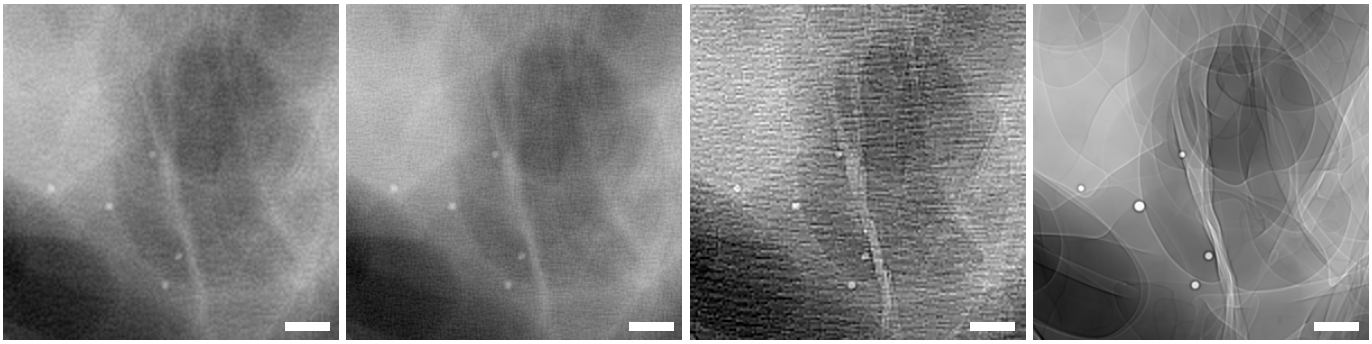

Fig. 7. Comparison of sampling strategies for simulation with mammography phantom. A subsection of the magnified section in Fig. 6 is shown at $R_1 = R_2 = 4$ m, resulting in an effective pixel size of 25 μm (cf. 50 μm in Fig. 6). To better show the sampling effects, no noise is included. (a) Phantom projected at the original voxelization (50 μm) with matched propagator sampling. (b) Higher propagator sampling ($\Delta x = 1.56$ μm) with matched phantom sampling by nearest-neighbor interpolation. (c) Same as in (b) but with bicubic interpolation applied to the projected phantom. (d) Proposed upsampling strategy consisting of interpolation in the 3D domain followed by projection. The grayscale window is set to [1.8, 2.2]. Scale bars are 1 mm.

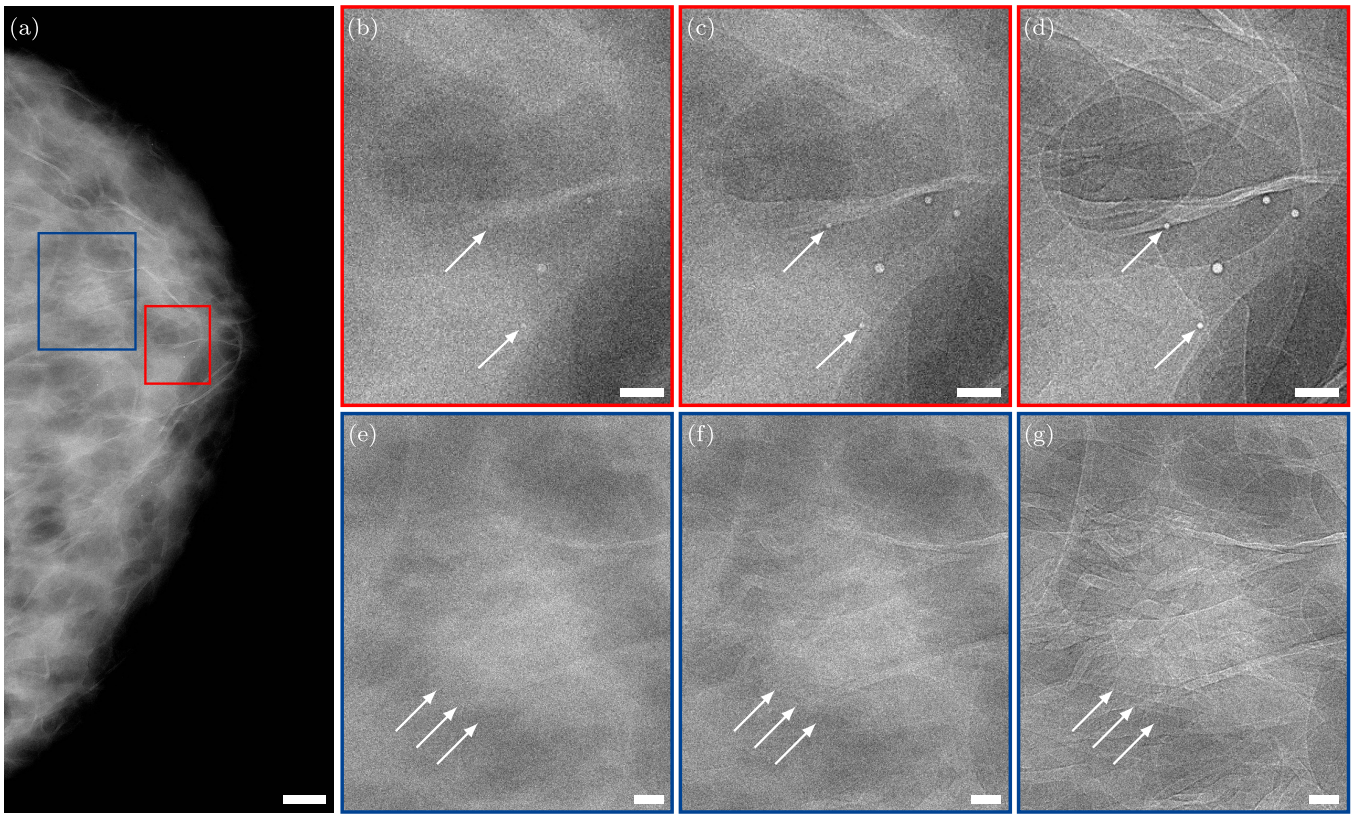

Fig. 8. WP simulation of PBI mammography with a state-of-the-art micro-focus source. Three effective propagation distances are shown, 0.5 m, 2 m, and 5 m, all with mean glandular dose of 1.5 mGy. Images are displayed as OD and grayscale is displayed in the range [1.5, 2.5]. (a) overview with $z_{\text{eff}} = 2$ m. Scale bar is 5 mm. (b)-(g) show the two magnified sections in (a) marked in red and blue for increasing distances. Scale bars are 1 mm. For (b) and (e) the distance will not produce significant phase contrast. For longer z_{eff} the edge enhancement associated with PBI is clearly visible. In (b)-(d) arrows mark two calcifications. In (e)-(g) a spiculated lesion is gradually more visible.

The upsampling strategy will make structures smooth and rounded but the real micro structure might have more edges. In practice, however, this works well for biological tissue as it is typically rounded on a larger scale. Smoothing can however be adjusted separately for each material if irregular features are needed. Features that are just a few voxels in the original phantom can be harder to properly adjust. Another issue is whether a sharp transition in material accurately represents biological tissue on the micrometer-level. While a sharp material transition is not unrealistic due to different cell types in different materials, the shape of the boundary might be differently textured. This texture, which could be introduced in the 4th processing step, should give a small decrease in phase contrast. This is an open question on how material boundaries should be modeled on a cellular and subcellular level and how that affects phase contrast.

For the projection step, cone-beam or parallel-beam geometry may be used. For simplicity and computational speed, we have modelled the latter (z-direction, cf. Fig. 2(a)) which is typically found at synchrotrons. A parallel geometry is

also useful as changes in phase contrast due to z are not mixed with changes in perspective. A cone-beam projection would furthermore have to be recomputed for every new choice of geometry. Nevertheless, the choice of projection geometry only results in a slight change in perspective of the projected phantoms. This is evident from Fig. 6 as our WP uses parallel beam whereas the MC simulation uses cone-beam. Tomography can be accomplished by projecting the upsampled phantom in multiple directions. Non-orthogonal projections (e.g., cone-beam) are also more computationally expensive compared to orthogonal projections (e.g., parallel-beam).

The use of WP instead of MC simplifies implementation and modification of simulations. Simulation speed is also typically to WP's advantage. MC computational time scales with photon count whereas WP scales mainly with transmission function sampling and number of energies simulated. Simulating many energies can thus be time consuming with WP, but in practice a few selected energies give an accurate simulation. Another important difference between MC and WP is simulation of scattering. MC does this accurately while the proposed method only accounts for the attenuation due to scattering. PBI has, however, a smaller scattering problem due to the propagation distance. Efficient scattering grids are also standard in mammography systems and other clinical imaging. So despite WP's more simplistic approach the result is very similar as shown in Sec. III-A.

All simulated images are displayed as OD ($-log(I/I_0)$). This is quite close to the raw data, and at the same time a bit more similar to clinical images. Mammography uses, however, post-processing algorithms that enhance certain features and give the images a look distinctly different from the raw data. This can be incorporated in the simulation framework, but was omitted as there is no standard for phase-contrast mammography. PBI data is often phase retrieved, but as the purpose of Fig. 7 and Fig. 8 is to show the conditions to achieve phase contrast, leaving the edge enhancement simplifies evaluation.

The simulation of a laboratory mammography system showed a clear contrast improvement for long propagation distances, but the exposure times required with the proposed X-ray source are too long and therefore not currently feasible for clinical imaging. While a thorough discussion on the feasibility of laboratory PBI mammography is outside the scope of this work, it is worth noting that the presented dose and source configuration are not optimized and that development of high-power micro-focus X-ray sources is under way.

In conclusion, we demonstrated how *in silico* propagation-based phase-contrast imaging is limited by a sampling requirement, but how existing coarsely voxelated phantoms can be processed to enable fast, realistic WP simulations.

A MATLAB implementation of the presented strategy and an upsampled phantom is available at https://github.com/ilianhaggmark/phase-contrast-phantom.

ACKNOWLEDGMENT

The authors would like to thank the PDC Center for High Performance Computing at the KTH Royal Institute of Technology for the computational resources, Anna Burvall (KTH) for comments of the manuscript, and Fredrik Strand (Karolinska Institute) & Dimitra Ntoula (Karolinska University Hospital) for comments on clinical aspects of mammography.

H. M. Hertz is a shareholder in Excillum AB.

REFERENCES

[1] S. T. Taba *et al.*, "Propagation-based phase-contrast CT of the breast demonstrates higher quality than conventional absorption-based CT even at lower radiation dose," *Academic Radiol.*, to be published, doi: 10.1016/j.acra.2020.01.009.

[2] S. W. Wilkins, T. E. Gureyev, D. Gao, A. Pogany, and A. W. Stevenson, "Phase-contrast imaging using polychromatic hard X-rays," *Nature*, vol. 384, no. 6607, pp. 335–338, Nov. 1996.

[3] E. Burattini *et al.*, "Mammography with synchrotron radiation," *Radiology*, vol. 195, pp. 239–244, Apr. 1995.

[4] F. Arfelli *et al.*, "Low-dose phase contrast X-ray medical imaging," *Phys. Med. Biol.*, vol. 43, pp. 2845–2852, Oct. 1998.

[5] F. Arfelli *et al.*, "Mammography with synchrotron radiation: Phase-detection techniques," *Radiology*, vol. 215, pp. 286–293, Apr. 2000.

[6] E. Castelli *et al.*, "Mammography with synchrotron radiation: First clinical experience with phase-detection technique," *Radiology*, vol. 259, no. 3, pp. 684–694, Jun. 2011.

[7] T. Tanaka *et al.*, "The first trial of phase contrast imaging for digital full-field mammography using a practical molybdenum X-ray tube," *Investigative Radiol.*, vol. 40, no. 7, pp. 385–396, Jul. 2005.

[8] T. Morita, M. Yamada, A. Kano, S. Nagatsuka, C. Honda, and T. Endo, "A comparison between film-screen mammography and full-field digital mammography utilizing phase contrast technology in breast cancer screening programs," in *Digital Mammography*, E. A. Krupinski, Ed. Berlin, Germany: Springer, 2008, pp. 48–54.

[9] M. Stampanoni *et al.*, "The first analysis and clinical evaluation of native breast tissue using differential phase-contrast mammography," *Investigative Radiol.*, vol. 46, no. 12, pp. 801–806, Dec. 2011.

[10] A. Olivo *et al.*, "Low-dose phase contrast mammography with conventional X-ray sources," *Med. Phys.*, vol. 40, no. 9, Aug. 2013, Art. no. 090701.

[11] C. Arboleda *et al.*, "Towards clinical grating-interferometry mammography," *Eur. Radiol.*, vol. 30, no. 3, pp. 1419–1425, Aug. 2019.

[12] F. Salvat, J. M. Fernández-Varea, and J. Sempau, "Penelope-2006: A code system for monte carlo simulation of electron and photon transport," in *Proc. Workshop*, Paris, France: Nuclear Energy Agency, Organization for Economic Co-operation and Development, vol. 4, 2006, p. 7.

[13] S. Agostinelli *et al.*, "Geant4—A simulation toolkit," *Nucl. Instrum. Meth. A*, vol. 506, pp. 250–303, Jul. 2003.

[14] T. T. Böhlen *et al.*, "The FLUKA code: Developments and challenges for high energy and medical applications," *Nucl. Data Sheets*, vol. 120, pp. 211–214, Jun. 2014.

[15] Z. Wang, Z. Huang, L. Zhang, Z. Chen, and K. Kang, "Implement X-ray refraction effect in Geant4 for phase contrast imaging," in *Proc. IEEE Nucl. Sci. Symp. Conf. Rec. (NSS/MIC)*, Oct. 2009, pp. 2395–2398.

[16] S. Cipiccia, F. A. Vittoria, M. Weikum, A. Olivo, and D. A. Jaroszynski, "Inclusion of coherence in monte carlo models for simulation of X-ray phase contrast imaging," *Opt. Express*, vol. 22, pp. 23480–23488, Sep. 2014.

[17] S. Peter *et al.*, "Combining Monte Carlo methods with coherent wave optics for the simulation of phase-sensitive X-ray imaging," *J. Synchrotron Radiat.*, vol. 21, no. 3, pp. 613–622, May 2014.

[18] E. Abadi *et al.*, "Virtual clinical trials in medical imaging: A review," *J. Med. Imag.*, vol. 7, no. 4, Apr. 2020, Art. no. 042805.

[19] M.-C. Gosselin *et al.*, "Development of a new generation of high-resolution anatomical models for medical device evaluation: The virtual population 3.0," *Phys. Med. Biol.*, vol. 59, no. 18, pp. 5287–5303, Aug. 2014.

[20] W. P. Segars, G. Sturgeon, S. Mendonca, J. Grimes, and B. M. W. Tsui, "4D XCAT phantom for multimodality imaging research," *Med. Phys.*, vol. 37, no. 9, pp. 4902–4915, Aug. 2010.

[21] M. I. Iacono *et al.*, "MIDA: A multimodal imaging-based detailed anatomical model of the human head and neck," *PLoS ONE*, vol. 10, no. 4, Apr. 2015, Art. no. e0124126.

[22] C. G. Graff, "A new, open-source, multi-modality digital breast phantom," *Proc. SPIE*, vol. 9783, Mar. 2016, Art. no. 978309.

[23] Y. Sung, W. P. Segars, A. Pan, M. Ando, C. J. R. Sheppard, and R. Gupta, "Realistic wave-optics simulation of X-ray phase-contrast imaging at a human scale," *Sci. Rep.*, vol. 5, no. 1, Jul. 2015, Art. no. 12011.

[24] B. Włodarczyk and J. Pietrzak, "Analytical reconstructions of intensity modulated X-ray phase-contrast imaging of human scale phantoms," *Biomed. Opt. Express*, vol. 6, no. 11, p. 4255, Oct. 2015.

[25] J. Wolf *et al.*, "Fast one-dimensional wave-front propagation for X-ray differential phase-contrast imaging," *Biomed. Opt. Express*, vol. 5, pp. 3739–3747, Oct. 2014.

[26] K. Bliznakova *et al.*, "A software platform for phase contrast X-ray breast imaging research," *Comput. Biol. Med.*, vol. 61, pp. 62–74, Jun. 2015.

[27] J. W. Goodman, *Introduction to Fourier Optics*, 3th ed. Greenwood, CO, USA: Roberts & Company, 2004.

[28] A. Pogany, D. Gao, and S. W. Wilkins, "Contrast and resolution in imaging with a microfocus X-ray source," *Rev. Sci. Instrum.*, vol. 68, no. 7, pp. 2774–2782, Jul. 1997.

[29] S. C. Mayo *et al.*, "Quantitative X-ray projection microscopy: Phase-contrast and multi-spectral imaging," *J. Microsc.*, vol. 207, no. 2, pp. 79–96, Aug. 2002.

[30] T. E. Gureyev, Y. I. Nesterets, A. W. Stevenson, P. R. Miller, A. Pogany, and S. W. Wilkins, "Some simple rules for contrast, signal-to-noise and resolution in in-line X-ray phase-contrast imaging," *Opt. Express*, vol. 16, no. 5, pp. 3223–3241, 2008.

[31] K. S. Morgan, K. K. W. Siu, and D. M. Paganin, "The projection approximation and edge contrast for X-ray propagation-based phase contrast imaging of a cylindrical edge," *Opt. Express*, vol. 18, pp. 9865–9878, May 2010.

[32] K. S. Morgan, K. K. W. Siu, and D. M. Paganin, "The projection approximation versus an exact solution for X-ray phase contrast imaging, with a plane wave scattered by a dielectric cylinder," *Opt. Commun.*, vol. 283, no. 23, pp. 4601–4608, Dec. 2010.

[33] A. Badano *et al.*, "Evaluation of digital breast tomosynthesis as replacement of full-field digital mammography using an in silico imaging trial," *JAMA Netw. Open*, vol. 1, no. 7, Nov. 2018, Art. no. e185474.

[34] U. Lundström *et al.*, "X-ray phase contrast for CO_2 microangiography," *Phys. Med. Biol.*, vol. 57, pp. 2603–2617, Apr. 2012.

[35] L. Kissel, "RTAB: The Rayleigh scattering database," *Radiat. Phys. Chem.*, vol. 59, no. 2, pp. 185–200, Aug. 2000.

[36] A. Badal and A. Badano, "Monte Carlo simulation of X-ray imaging using a graphics processing unit," in *Proc. IEEE Nucl. Sci. Symp. Conf. Rec. (NSS/MIC)*, Oct. 2009, pp. 4081–4084.

[37] J. M. Boone, T. R. Fewell, and R. J. Jennings, "Molybdenum, rhodium, and tungsten anode spectral models using interpolating polynomials with application to mammography," *Med. Phys.*, vol. 24, no. 12, pp. 1863–1874, Dec. 1997.

[38] U. Bick and F. Diekmann, *Digital Mammography*. Berlin, Germany: Springer, 2010.

[39] I. Amendoeira *et al.*, *European Guidelines for Quality Assurance in Breast Cancer Screening and Diagnosis*. Brussels, Belgium: European Commission, 2013.

[40] J. T. Bushberg, J. A. Seibert, E. M. Leidholdt, and J. M. Boone, *The Essential Physics of Medical Imaging*, 3th ed. Norwell, MA, USA: Kluwer, 2012.

[41] C. Rakete *et al.*, "Compact X-ray microradiograph for *in situ* imaging of solidification processes: Bringing *in situ* X-ray micro-imaging from the synchrotron to the laboratory," *Rev. Sci. Instrum.*, vol. 82, no. 10, Oct. 2011, Art. no. 105108.

[42] J. B. Tiller, A. Barty, D. Paganin, and K. A. Nugent, "The holographic twin image problem: A deterministic phase solution," *Opt. Commun.*, vol. 183, nos. 1–4, pp. 7–14, Sep. 2000.

[43] P. C. Johns and M. J. Yaffe, "X-ray characterisation of normal and neoplastic breast tissues," *Phys. Med. Biol.*, vol. 32, no. 6, pp. 675–695, Jun. 1987.

[44] A. Piai *et al.*, "Quantitative characterization of breast tissues with dedicated CT imaging," *Phys. Med. Biol.*, vol. 64, no. 15, Aug. 2019, Art. no. 155011.

[45] P. Butler, A. Mitchell, and J. C. Healy, eds., *Applied Radiological Anatomy*, 2nd. ed. Cambridge, U.K.: Cambridge Univ. Press, 2012.